Research Article | Vol. 26, No. 12 | 11 Jun 2018 | OPTICS EXPRESS 14959
Optics EXPRESS

Mach-Zehnder crossbar switching and tunable filtering using N-coupled waveguide Bragg resonators

RICHARD A. SOREF,[1] FRANCESCO DE LEONARDIS,[2] AND VITTORIO M. N. PASSARO[2,*]

[1]*Department of Engineering, The University of Massachusetts, Boston, Massachusetts 02125, USA*
[2]*Photonics Research Group, Dipartimento di Ingegneria Elettrica e dell'Informazione, Politecnico di Bari, Via Edoardo Orabona n. 4, 70125 Bari, Italy*
**vittorio.passaro@poliba.it*

Abstract: This theoretical modeling-and-simulation paper presents designs and projected performance of ~1500-nm silicon-on-insulator 2 x 2 Mach-Zehnder interferometer (MZI) optical crossbar switches and tunable filters that are actuated by thermo-optical (TO) means. A TO heater stripe is assumed to be on the top of each waveguided arm in the interferometer. Each strip-waveguide arm contains an inline set of N-fold coupled, phase-shifted Bragg-grating resonators. To implement accurate and realistic designs, a mixed full-vectorial mathematical model based upon the finite-element, coupled-mode, and transfer-matrix approaches was employed. The Butterworth-filter technique for grating length and weighting was used. The resulting narrowband waveguide-transmission spectral shape was better-than-Lorentzian because of its steeper sidewalls (faster rolloff). The metrics of crossbar switching, insertion loss (IL) and crosstalk (CT), were evaluated for choices of grating strength and TO-induced change in the grating-waveguide refractive index. The predicted ILs and CTs were quite superior to those cited in the literature for experimental and theoretical MZI devices based upon silicon nanobeam resonators. This was true for the Type-I and Type-II resonator addressing discussed here. Finally, we examined the TO-tunable composite filter profiles that are feasible by connecting two or more Type-I MZIs in an optical series arrangement. A variety of narrow filter shapes, tunable over ~2 nm, was found.

OCIS codes: (230.4555) Coupled resonators; (250.6715) Switching; (130.7408) Wavelength filtering devices; (230.1480) Bragg reflectors.

References and links

1. C. Doerr, "Silicon photonic integration in telecommunications," Front. Phys. **3**, 7 (2015).
2. Y. Li, Y. Zhang, L. Zhang, and A. W. Poon, "Silicon and hybrid silicon photonic devices for intra-datacenter applications: state of the art and perspectives," Photon. Res. **3**(5), B10–B27 (2015).
3. Q. Xu and R. Soref, "Reconfigurable optical directed-logic circuits using microresonator-based optical switches," Opt. Express **19**(6), 5244–5259 (2011).
4. C. Qui, W. Gao, R. Soref, J. Robinson, and Q. Xu, "Demonstration of reconfigurable electro-optical directed-logic circuit using carrier-depletion micro-ring resonators," in *CLEO Science and Innovations* (2015), paper SM2I.4.
5. H. Zhou, C. Qiu, X. Jiang, Q. Zhu, Y. He, Y. Zhang, Y. Su, and R. Soref, "Compact, submilliwatt 2 x 2 silicon thermo-optic switch based on photonic crystal nanobeam cavities," Photon. Res. **5**(2), 108–112 (2017).
6. X. Jiang, H. Zhang, C. Qiu, Y. Zhang, Y. Su, and R. Soref, "Compact and power-efficient 2 x 2 thermo-optical switch based on the dual-nanobeam MZI," in *Optical Fiber Communication Conference* (2018), paper Th2A.7.
7. R. Soref, "Resonant and slow-light 2 x 2 switches enabled by nanobeams and grating-assisted waveguides," in *Progress in Electromagnetics Research Symposium* (2017), paper IP5.9.
8. R. Soref, "Tutorial: Integrated- Photonic Switching Structures," APL Photonics **3**(2), 021101 (2018).
9. V. Veerasubramanian, G. Beaudin, A. Giguère, B. Le Drogoff, V. Aimez, and A. G. Kirk, "Waveguide-coupled drop filters on SOI using quarter-wave shifted sidewalled grating resonators," Opt. Express **20**(14), 15983–15990 (2012).
10. R. Soref and J. Hendrickson, "Proposed ultralow-energy dual photonic-crystal nanobeam devices for on-chip N x N switching, logic, and wavelength multiplexing," Opt. Express **23**(25), 32582–32596 (2015).

#326617 https://doi.org/10.1364/OE.26.014959
Journal © 2018 Received 21 Mar 2018; revised 2 May 2018; accepted 2 May 2018; published 29 May 2018

Optics EXPRESS

11. J. R. Hendrickson, R. Soref, and R. Gibson, "Improved 2 × 2 Mach-Zehnder switching using coupled-resonator photonic-crystal nanobeams," Opt. Lett. **43**(2), 287–290 (2018).
12. R. Soref, J. R. Hendrickson, and J. Sweet, "Simulation of germanium nanobeam electro-optical 2 × 2 switches and 1 × 1 modulators for the 2 to 5 mm infrared region," Opt. Express **24**(9), 9369–9382 (2016).
13. H. Zhou, C. U. Qi, X. Jiang, Q. Zhu, Y. He, Y. Su, and R. Soref, "Compact, submilliwatt 2 × 2 silicon thermos-optic switch based on photonic crystal nanobeam cavities," Photon. Res. **5**(2), 108–112 (2017).
14. W. Zhang and J. Yao, "Silicon-based integrated microwave photonics," IEEE J. Quantum Electron. **52**, 1–12 (2016).
15. Y. Xie, Z. Gen, L. Zhuang, M. Burla, C. Taddei, M. Hoekman, A. Leinse, C. G. H. Roeloffzen, K.-J. Boller, and A. J. Lowery, "Programmable optical processor chips: toward photonic RF filters with DSP-level flexibility and MHz-band selectivity," Nanophotonics **7**, 1–34 (2017).
16. J. Capmany and P. Muñoz, "Integrated microwave photonics for radio access networks," J. Lightwave Technol. **32**(16), 2849–2861 (2014).
17. M. Burla, X. Wang, M. Li, L. Chrostowski, and J. Azaña, "Wideband dynamic microwave frequency identification system using a low-power ultracompact silicon photonic chip," Nat. Commun. **7**, 13004–13012 (2016).
18. M. Spasojevic and L. R. Chen, "Tunable optical delay line in SOI implemented with step chirped Bragg gratings and serial grating arrays," Proc. SPIE **8915**, 89150S (2013).
19. A. D. Simard and S. LaRochelle, "Complex apodized Bragg grating filters without circulators in silicon-on-insulator," Opt. Express **23**(13), 16662–16675 (2015).
20. S. LaRochelle, A. D. Simard, "Silicon Photonic Bragg Grating Devices," in OFC (2017), paper Th1G.3.
21. X. Wang and C. K. Madsen, "Highly sensitive compact refractive index sensor based on phase-shifted sidewall Bragg gratings in slot waveguide," Appl. Opt. **53**(1), 96–103 (2014).
22. M. Burla, H. P. Bazargani, and J. St-Yves, 2, W. Shi, L. Chrostowski, J. Azaña, "Frequency Agile Microwave Photonics Notch Filter based on a Waveguide Bragg Grating on Silicon," in *Int. Topic Meeting on Microwave Photonics and 9th Asia-Pacific Microwave Photonics* (2014), pp. 392–394.
23. Z. Chen, J. Flueckiger, X. Wang, F. Zhang, H. Yun, Z. Lu, M. Caverley, Y. Wang, N. A. F. Jaeger, and L. Chrostowski, "Spiral Bragg grating waveguides for TM mode silicon photonics," Opt. Express **23**(19), 25295–25307 (2015).
24. X. Wang, W. Shi, R. Vafaei, N. A. F. Jaeger, and L. Chrostowski, "Uniform and Sampled Bragg Gratings in SOI Strip Waveguides With Sidewall Corrugations," IEEE Photonics Technol. Lett. **23**, 290–292 (2011).
25. J. Jiang, H. Qiu, G. Wang, Y. Li, T. Dai, X. Wang, H. Yu, J. Yang, and X. Jiang, "Broadband tunable filter based on the loop of multimode Bragg grating," Opt. Express **26**(1), 559–566 (2018).
26. B. Troia, F. De Leonardis, and V. M. N. Passaro, "Generalized modelling for the design of guided-wave optical directional couplers," Opt. Lett. **39**(5), 1161–1164 (2014).
27. V. M. N. Passaro, R. Loiacono, G. D'Amico, and F. De Leonardis, "Design of Bragg Grating Sensors Based on Submicrometer Optical Rib Waveguides in SOI," IEEE Sens. J. **8**(9), 1603–1611 (2008).
28. S. Ramo, J. R. Whinnery, and T. Van Duzer, *Fields and Waves in Communications Electronics* (John Wiley & Sons, Inc., 1995).
29. R. Soref, F. De Leonardis, V. M. N. Passaro, "Reconfigurable optical-microwave filter banks using thermo-optically tuned Bragg Mach-Zehnder devices," Opt. Express, in publication.
30. L. Lu, L. Zhou, X. Li, and J. Chen, "Low-power 2×2 silicon electro-optic switches based on double-ring assisted Mach-Zehnder interferometers," Opt. Lett. **39**(6), 1633–1636 (2014).
31. Z. Guo, L. Lu, L. Zhou, L. Shen, and J. Chen, "16 × 16 Silicon Optical Switch Based on Dual-Ring-Assisted Mach–Zehnder Interferometers," J. Lightwave Technol. **36**(2), 225–232 (2018).

1. Introduction

This theoretical modeling-and-simulation paper deals with resonant-structure innovations and major improvements in the predicted performance of narrowband 2 x 2 Mach-Zehnder crossbar switches that are actuated by thermo-optical (TO) means. This TO control offers relatively large (albeit slow) perturbation of the resonator's effective index Δn, and the TO switches offer proof-of-principle for the ultrafast electro-optical (EO) crossbar versions. The corresponding EO 2 x 2s would use a free-carrier Δn mechanism such as depletion of PN-doped resonators.

Within the realm of integrated photonics, such as on-chip silicon photonics, these narrowband 2 x 2s are newcomers compared to the established broadband MZIs. The resonant 2 x 2s find application in datacomm/telecomm [1,2] where such 2 x 2s would often be interconnected to form an N x N matrix switch within a wavelength-multiplexed system. The resonant N x Ns solve the problem of ultralow-energy switching, but they require several tradeoffs or compromises in the system. Electro-optical logic [3,4] is another good application of the narrow (EO-type) MZIs discussed here.

Optics EXPRESS

Only a few experiments have been performed on resonant 2 x 2 MZIs [5,6] and those used silicon nanobeams in the interferometer arms. The waveguided Bragg grating (WBG) is analogous to the nanobeam lattice, and a Bragg device can perform "nanobeam tasks" [7–9] when two WBGs are joined with a short phase-shift segment to form a waveguide Bragg resonator (WBR). This resonance can then be shifted along the wavelength axis in the same manner as for the nanobeam resonance [10–13]. The possibilities for engineering the WBR are arguably more numerous than they are for nanobeams. In the context of spatial routing switches, very little theory exists on the WBRs and this deficiency is addressed in this paper. When engineered–as discussed here–we find WBRs to be versatile and competent as both switches and tunable filters. A new strategy set forth here is to couple closely two or more Bragg cavities in one strip waveguide. The resulting normal modes give one spectral profile for the N-coupled-cavity waveguide. This advantageous new profile is non-Lorentzian with steep roll-off of the side walls, and its bandpass is adjustable. With numerical methods presented here, the optimized WBR MZI affords outstanding metrics in its optical insertion loss IL and optical crosstalk CT. The N-coupled WBR approach gives many choices of filter shape and the MZI footprint is reasonably compact for $N \leqq 4$ and thereby practical.

The MZI designer has the freedom to choose the central resonance wavelength of the WBR in each arm of the MZI, that is, to select λ_1 and λ_2. With the TO heaters off, those wavelengths can be the same or can be slightly different, as desired. These two situations ($\lambda_1 = \lambda_2$ and $\lambda_2 = \lambda_1 + \delta\lambda$) require different "addressing" of TO heaters to reach the cross and the bar states. We call these Type-I and Type-II addressings and these are explored here. Both types project excellent performance.

The MZI offers a passband filter at its Through port and a related notch filter (stop band filter) at its Drop port. Since the TO effect offers practical shifting of both profiles along the wavelength axis, the MZI is in effect a tunable-filter device and we are able to attain bandwidths in the range of a few GHz or tens of GHz. In this paper, we propose a new kind of filter-switch mesh in which two or more MZI variable filters are connected in cascade. Because several practical, tunable filter shapes become available in the cascade, our proposal implies that the TO MZI is useful in on-chip microwave photonics to filter the optical sidebands that are formed on an optical carrier signal when that light beam is amplitude-modulated by an RF input signal [14–16]. RF spectrum analysis and other functions such as frequency measurement of an unknown microwave frequency [17] can be performed by our tunable filter devices. Also feasible on the silicon filter chip are optical spectroscopy and optical sensing.

The photonics platform assumed here is the foundry-compatible and CMOS-compatible silicon-on-insulator (SOI) platform operating around 1550 nm. As mentioned, we investigate MZI arms composed of N-coupled WBRs.

The paper is organized as follows. Device architecture and numerical methods of simulating the device behaviour under different operative conditions are presented in Section 2. Then, in Section 3, general design guidelines and parametric simulations are reported for MZI crossbars. On-chip performance is projected as a function of signal wavelength, thermal tuning and grating strength. A comparison with the state-of-the-art is presented in Section 4. Finally, Section 5 summarizes the conclusions.

2. MZI device architecture and grating-engineering method

The 2 x 2 TO MZI building-block device analyzed here is in the ~1550-nm SOI platform. The strip waveguides have the width and height for single-mode operation, and we have deliberately chosen for the Bragg structures silicon side-corrugations or "teeth" that protrude outside of the width because this "outside" approach gives better performance than either the "inside" or "mixed" corrugation approaches. The resulting Bragg devices are versatile and have a number of different applications as is illustrated by the state-of-the-art Bragg-structure

Optics EXPRESS

applications in the literature [17–25]. Figures 1(a) and 1(b) show the architecture and the schematic black box, respectively.

The device consists of N waveguide Bragg resonators end-coupled to each other in one waveguide, and such waveguides are placed in the two arms of the MZI. Directional couplers (DCs) are used as input and output devices. In particular, the coupler gap (G), and the directional coupler length (L_c) are designed to induce 3-dB behavior. Under this hypothesis, the outputs at the drop and through ports of the MZI are equal to the reflection and transmission of the N-coupled WBRs, respectively. The structure of the i-th resonator within the WBR channel is illustrated in Fig. 1(c), together with the fundamental geometrical parameters. Moreover, the MZI switch is physically realized on a SOI strip waveguide covered by silicon dioxide and having a width, W, and an height, H, as sketched in Fig. 1(d). As mentioned, tuning is actuated by TO heater strips deposited on the top of the WBRs, the orange stripes in Fig. 1(a). As outlined in [11], the TO technique can be considered as an efficient tool to induce refractive index changes (Δn) with low-power consumption (i.e., TO Off state $\Delta n = 0$, TO On state $\Delta n \neq 0$). Indeed, the temperature increase required to obtain $\Delta n = 0.0015$ is about 8 K, due to silicon's thermo-optic coefficient $dn/dT = 1.86 \times 10^{-4}$ K^{-1}. The ΔT required to achieve $\Delta n = 0.004$ is not excessive and is also included below.

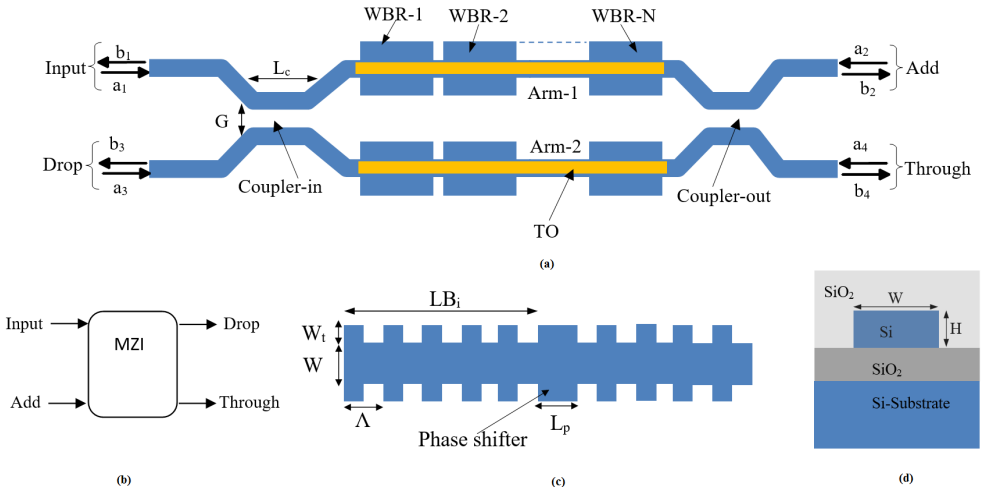

Fig. 1. (a) Schematic architecture of on-chip 2 × 2 MZI switch (in orange the heating strips). (b) 2 × 2 MZI switch black box; (c) i-th waveguide Bragg resonator; (d) SOI waveguide cross section.

The DC and WBG design and simulations require very robust mathematical models to be as flexible and accurate as possible. For that purpose, several approaches have been investigated and traditionally implemented. The two-dimensional (2D) and three-dimensional (3D) beam propagation method (BPM) and the finite-difference time-domain (FDTD) method are widely used for simulation and design of DCs and WBGs. Those approaches allow us to determine the overall device operation. However, the BPM and FDTD methods are well known to be time- and memory-consuming, thus not suitable for simulating long devices or multi-waveguide sections, and the methods suffer from divergence of numerical solutions. This aspect could be considered a drawback when the switch design rules have to be deduced from several parametric simulations. In this context, the implementation of a mixed numerical approach based on the finite-element method (FEM) and full vectorial coupled-mode theory (CMT) can provide a better approach for the flexible simulation and design of DCs and WBGs. Indeed, comparisons with 3D-BPM [26] and rigorous Floquet-Bloch theory [27] have demonstrated the good accuracy of this mixed approach which is adopted here.

Optics EXPRESS

After the determination of the coupling coefficient, the amplitude reflectivity and transmittivity for each Bragg section of length LB_i, the waveguide Bragg resonator has been simulated by means of the transfer matrix approach. However, with the aim of setting up a mathematical tool useful to analyze cascaded MZIs with different configurations and operational conditions, we characterize the 2 × 2 MZI switch as in Eq. (1):

$$\begin{bmatrix} b_2 \\ a_2 \\ b_4 \\ a_4 \end{bmatrix} = \boldsymbol{T}_{MZI} \begin{bmatrix} b_1 \\ a_1 \\ b_3 \\ a_3 \end{bmatrix} = \boldsymbol{T}_c \boldsymbol{T}_{arm} \boldsymbol{T}_c \begin{bmatrix} b_1 \\ a_1 \\ b_3 \\ a_3 \end{bmatrix} \tag{1}$$

where the $\boldsymbol{T}_{MZI}$ is the global 4 × 4 transfer matrix of the 2 × 2 MZI switch, and the terms b_i and a_i represent the outcoming and the incoming field amplitudes at the generic MZI port [Fig. 1(a)], respectively. Similarly, $\boldsymbol{T}_{arm}$ is the 4x4 transfer matrix related to the two MZI arms given by:

$$\boldsymbol{T}_{arm} = \begin{bmatrix} \boldsymbol{T}_{arm1} & 0 \\ 0 & \boldsymbol{T}_{arm2} \end{bmatrix} \tag{2}$$

The 2 × 2 matrices $\boldsymbol{T}_{arm1}$, and $\boldsymbol{T}_{arm2}$ represent the transfer matrices of the MZI arm-1 and arm-2, respectively, depending on the WBR structure and taking into account both forward and backward waves. Thus, in the context of the transfer matrix approach, the matrix product defined in Eq. (1) can be performed by using the general formalism for which incoming and outcoming field are present at each DC port. In this sense, the DC transfer matrix $\boldsymbol{T}_c$ is given by [20]:

$$\boldsymbol{T}_c = \begin{bmatrix} \boldsymbol{A} & \boldsymbol{B} \\ \boldsymbol{C} & \boldsymbol{D} \end{bmatrix} = \begin{bmatrix} S_{12} & 0 & S_{23} & 0 \\ 0 & \dfrac{S_{34}}{S_{12}S_{34} - S_{14}S_{23}} & 0 & \dfrac{-S_{14}}{S_{12}S_{34} - S_{14}S_{23}} \\ S_{14} & 0 & S_{34} & 0 \\ 0 & \dfrac{-S_{23}}{S_{12}S_{34} - S_{14}S_{23}} & 0 & \dfrac{S_{12}}{S_{12}S_{34} - S_{14}S_{23}} \end{bmatrix} \tag{3}$$

where, the 2 × 2 matrices $\boldsymbol{A}$, $\boldsymbol{B}$, $\boldsymbol{C}$,and $\boldsymbol{D}$, are extracted from the DCs transfer matrix, and S_{ij} are the DC scattering matrix elements as a function of the the amplitude coupler and transmission factors [28].

3. Numerical results

The 2 x 2 crossbar switch is investigated in this section, and after that a brief sketch of tunable optical filtering by MZIs is given. For the crossbar, the wavelength of operation λ_0 is near 1550 nm.

With reference to Figs. 1(c) and 1(d), the filter is physically realized with WBRs in a SOI wire waveguide having unperturbed cross section of W = 450 nm width and H = 250 nm thickness. The Bragg grating sections are created by introducing along the nanowire, sidewall corrugations having width extension (W_t) ranging from 50 to 100 nm. The period is chosen to be Λ = 315 nm in order to operate at the central wavelength of 1550 nm. Moreover, the phase-shift sections each with a length L_p = 315 nm (at W_t = 100 nm) are included in the middle of each WBR in order to induce a narrow transmission-filter behavior with 3-dB

Optics EXPRESS

bandwidth (BW). Hereafter, we focus the design and analysis on the TE polarization, specifically the TE_{00} fundamental optical mode. In addition, the generalized model implemented makes it possible to simulate and design any desired DCs; for example, input and ouput DCs based upon the geometry sketched in Fig. 1(a) have been employed in this investigation. Thus, a coupler length L_c = 22.82 μm is required to realize the 3-dB mechanism if a coupler gap G = 250 nm is assumed. However, it is worth noting that the following analysis can be also carried out in the case of SOI-based rib waveguides, but simulation results have revealed that the effective modal areas increase exponentially as a function of shallower Si-core etch depth, thus confirming the fully-etched waveguides as being most suitable for achieving low power tunability while assuming the TO heater on the top of the optical waveguide.

In the WBR, the phase-shifted Bragg grating acts as an optical resonator storing electromagnetic energy and communicating to the outputs through either port constituted by the two Bragg grating sections. Thus, it leaks energy through either side via its exponential tails. In this context, this power escape can be characterized by a decay rate $1/\tau_l$, where the term τ_l is the photon lifetime inside the optical resonator. Therefore, it is possible to demonstrate that the relationship $1/\tau_l \propto e^{-2|\kappa_c|\cdot LB}$ holds, where κ_c is the coupling coefficient between the forward and backward modes inside the Bragg grating. In this context, the CMT in the time domain can represent an alternative approach to study the WBR structures. Simulations indicates that the spectral response calculated by the CMT time domain faithfully reproduces the response obtained by means of the mixed numerical approach FEM/vectorial CMT-space domain, near the resonance. Further away from resonance, the two responses increasingly deviate. Despite this loss of accuracy, the CMT-time represents a powerful tool to demonstrate that, close to the resonance, the spectral response of the N-coupled WBR resonators is functionally equal to a standard LC ladder circuit. The LC ladder-circuit is a very well-studied circuit for which filter design tables exist. Thus, the WBR parameters, in particular the lengths LB_i, can be designed to get desired spectral responses such as Butterworth, Chebyschev, and Gaussian. Then, our optimization algorithm is organized as follows: first, the N-coupled resonators are analyzed at the resonance by means of the CMT-time in order to evaluate the lengths LB_i, and subsequently the mixed numerical approach based on the finite-element method and full vectorial CMT-space is adopted to perform more accurate spectral simulations. In this context, the lengths LB_i can be evaluated as:

$$LB_i = \frac{1}{2\kappa_c}\log\left(\frac{g_i}{g_1}\right) + LB_1; \quad i > 1 \tag{4}$$

where the terms g_i are the ladder-circuit normalized coefficients, as listed in Table 1.

Table 1. Ladder-circuit coefficients.

Butterworth response					
Values	g_1	g_2	g_3	g_4	g_5
N = 2	1.4142	1.4142			
N = 3	1	2	1		
N = 4	0.7654	1.8478	1.8478	0.7654	
N = 5	0.6180	1.6180	2	1.6180	0.6180
Chebyshev response 0.5 Ripple Band					
N = 2	1.4029	0.7071			
N = 3	1.5963	1.0967	1.5963		
N = 4	1.6703	1.1926	2.3661	0.8419	
N = 5	1.7058	1.2296	2.5408	1.2296	1.7058

Optics EXPRESS

Hereafter, we assume the length of the first WBR (LB_1) as a degree of freedom and express the subsequent lengths LB_1 with $i \neq 1$ as a function of LB_1 [Eq. (4)] in order to induce a maximally flat filter response. The parameters listed in Table 2 have been used to obtain the Butterworth filter response, and the N = 2 case, not shown, has $LB_1 = LB_2$ (see Table 1).

Table 2. Coupled Bragg resonators parameters.

Values	LB_1	LB_2	LB_3	LB_4	LB_5
N = 3	Parametric value	~1.3 × L_1	L_1	-	-
N = 4	Parametric value	~1.25 × L_1	~1.25 × L_1	L_1	-
N = 5	Parametric value	~1.3 × L_1	~1.35 × L_1	L_2	L_1

Hereafter, the length of the first Bragg resonator is given as $LB_1 = M \times \Lambda$, where M is the number of periods in the Bragg section of the first WBG [Figs. 1(a) and 1(c)]. Under the above-mentioned design conditions, we simulate in the following two different 2 × 2 MZI optical switches, designated as Type I and Type II. In the Type I device the MZI is symmetic having the WBRs of arm-1 and arm-2 [Fig. 1(a)] matched at the same resonance wavelengths ($\lambda_1 = \lambda_2 = \lambda_0$) with the TO heaters Off. An asymmetric arrangement is realized in the MZI-Type II [6], where the arms 1 and 2 are constructed, respectively with $\lambda_2 = \lambda_0$, and $\lambda_2 = \lambda_1 + \delta\lambda$ when the heaters are Off. The two TO heaters are addressed independently and a given heater is either On or Off. Then we need the following addressing of heaters to reach the following switch states: Type I: Cross = Off, Off; Bar = On, On. Type II: Cross = On, Off; Bar = Off, On.

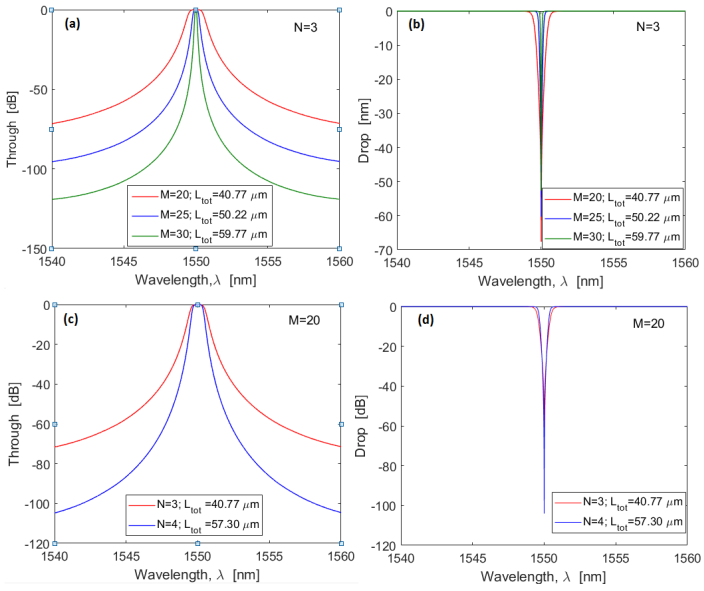

Fig. 2. (a) Through spectrum for different values of M, assuming N = 3; (b) Drop spectrum for different values of M, assuming N = 3; c) Through spectrum for N = 3, and N = 4, assuming M = 20; d) Drop spectrum for N = 3, and N = 4, assuming M = 20. The simulations are performed by considering: W = 450 nm, H = 250 nm, W_t = 100 nm, Λ = 315 nm, and α_l = 1 dB/cm.

Optics EXPRESS

The Through and Drop spectra are plotted in Figs. 2(a) and 2(b) for different values of the periods number M and for a fixed number N of coupled WBRs in each arm of the MZI-Type I, respectively.

In the simulations, we have assumed the corrugation width (W_t), and the amplitude propagation loss coefficient (α_l) of 100 nm and 1 dB/cm [23], respectively. Similarly, Figs. 2(c) and 2(d) show the Type I Through and Drop spectra for a fixed value of M, and changing N. Inspection of the Figure reveals that the response is maximally flat, and that the BW and rolls-off are N times narrower and faster than for $N = 1$. Thus, Figs. 2(a)-2(d) demonstrate that the desired BW and roll-off can be obtained by selecting opportunely both LB_1 and N. Some representative simulation results for $W_t = 80$ and 100 nm are summarized in Table 3, suggesting that the combination $M = 30$, and $N = 3$ is the condition for realizing a good trade-off between higher filter performance and small footprint. The information frequency bandwidth in Table 3 has also been stated in terms of GHz, indicating that the switch designer can readily "construct" a device anywhere in the 10 to 100 GHz range. Moreover, the results listed in Table 3 indicate that for a given footprint the filter bandwidth decreases by increasing the corrugation width (W_t) as a result of the enhancement of the coupling coefficient (κ_c) between the forward and backward modes inside the Bragg grating sections. Although further improvements can be obtained for W_t >100 nm, we assume in our investigations $W_t = 100$ nm as the trade-off between filter performances and standard lithographic process [17].

After attaining the above results, a parametric investigation of the switching mechanism in terms of IL and CT as a function of the TO-induced refractive index change (Δn) was carried out, for both cases of interest: i) $M = 30$, $N = 3$, and $W_t = 100$ nm; ii) $M = 30$, $N = 3$, and $W_t = 80$ nm. In this context, Figs. 3(a)-3(d) show the Type-I Through and Drop spectra for $\Delta n = 0.0015$ and 0.004, assuming $M = 30$, $N = 3$, and $W_t = 100$ (left panels), and = 30, N = 3, and $W_t = 80$ (right panels).

Table 3. Filter performance for MZI-Type I.

		Bandwidth (BW) [nm]	Bandwidth (BW) [GHz]	Roll-off [dB/nm]
$W_t = 100$ nm	$N = 3;\ M = 20$	1.05	131.1	22.9
	$N = 3;\ M = 25$	0.4	50.0	58.9
	$N = 3;\ M = 30$	0.15	18.7	150.5
	$M = 20;\ N = 4$	0.77	96.2	39.4
$W_t = 80$ nm	$N = 3;\ M = 20$	1.63	204.0	15.6
	$N = 3;\ M = 25$	0.71	88.7	35.7
	$N = 3;\ M = 30$	0.3	37.5	80
	$M = 20;\ N = 4$	1.28	159.8	27

Table 4. Calculated 2 x 2 switching performance for MZI-Type I.

		$N = 3;\ M = 30;\ W_t = 100$ nm	$N = 3;\ M = 30;\ W_t = 80$ nm
Insertion Loss (Cross) [dB]		–0.48	–0.26
Crosstalk (Cross) [dB]		–52.7	–52.9
Insertion Loss (Bar) [dB]	$\Delta n = 0.0015$	–0.01	–0.02
	$\Delta n = 0.004$	–0.002	–0.003
Crosstalk (Bar) [dB]	$\Delta n = 0.0015$	–50.5	–34.4
	$\Delta n = 0.004$	–75.6	–59.7

Optics EXPRESS

The main features of the 2 × 2 Type-I MZI crossbar switch operating at $\lambda_1 = \lambda_2 = \lambda_0 =$ 1550 nm are are then summarized in Table 4, where the insertion loss and the crosstalk parameters are extracted from the curves of Figs. 3(a)-3(d). The IL of the MZI device is the sum of the *N*-WBR IL cited in Table 3 and the loss of the other waveguides in the MZI.

Clearly, the larger TO index perturbation leads to superior IL and CT metrics. However, an important conclusion here is that the "small" 0.0015 perturbation already gives very high predicted performance, which is a good omen for EO devices.

Turning now to the Type-II MZI, we performed similar investigations with results presented in Figs. 4(a)-4(c), where the switching for Type-II was for the case $M = 30$, $N = 3$, $W_t = 100$, with $\delta\lambda = 1$ nm assumed.

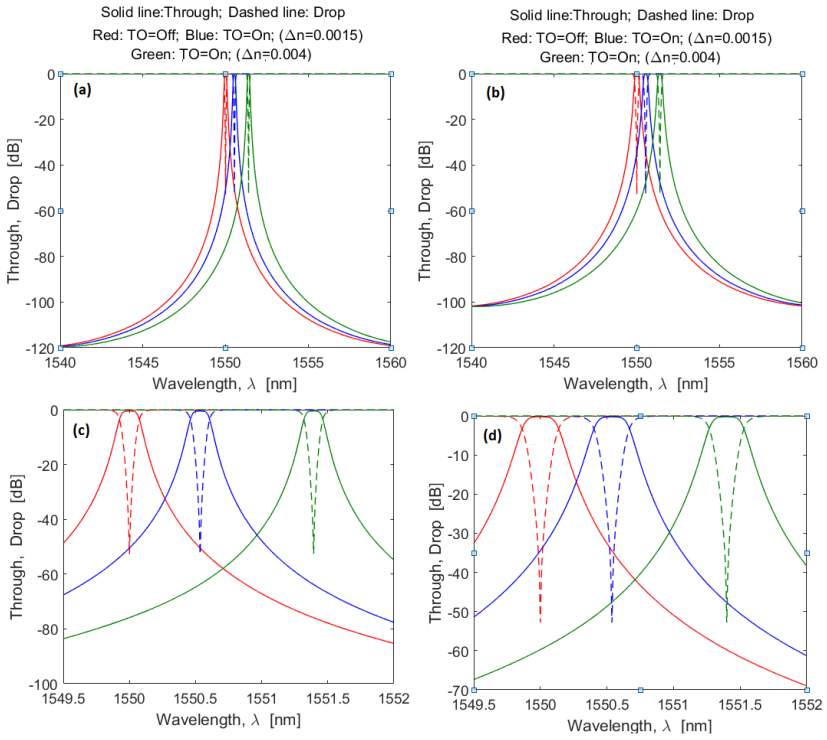

Fig. 3. Type-I Through and Drop spectra for $N = 3$, and $M = 30$, assuming $W_t = 100$ nm (left panels) and $W_t = 80$ nm (right panels); A zoom plot is shown in (c) and in (d). Red line represents the cross state, Blue and Green lines indicate the Bar state.

In particular, Fig. 4(a) indicates the predicted Through and Drop spectra for the Off, Off heater condition. In this context, the switching operative wavelength is set at $\lambda_o = \lambda_2 = 1551$ nm, while λ_1 is chosen at 1550 nm, that is, $\lambda_2 = \lambda_1 + \delta\lambda$, and the Cross state [Fig. 4(b)] is induced by switching-On TO_1 ($\Delta n_1 = 0.00285$) and by turning-Off TO_2. The BW in Fig. 4(b) is 17.4 GHz. The opposite (Off, On) condition is required to induce the Bar state [Fig. 4(c)]. Thus, from Figs. 4(a)-4(c), our results record IL and CT values of about –0.49 dB, and –52.6 dB, and –0.07 dB, and –85.3 dB for the Cross and Bar states, respectively, results that compare favorably with those in Table 4 and offer superiority to the literature. Figure 4(d) shows the TO-induced refractive index change needed for the Fig. 4(b)-Cross as a function of the $\delta\lambda$ choice up to 1.5 nm. However larger values $\delta\lambda$ of are possible by requiring $\Delta n >$ 0.004. For different selections of $\delta\lambda$, the insertion loss and crosstalk for both Cross and Bar

Optics EXPRESS

states are plotted in Figs. 4(e), and 4(f), respectively, excellent performance that increases with increasing δλ.

If dimensional errors $\Delta\Lambda$ are made in fabricating the period, the resonance will be affected. Indeed, each resonator in the N-coupled WBR has its individual resonance wavelength which must be aligned to attain optimum performance in terms of metrics and spectral profile. However, in practice, errors in fabrication can induce misalignments in resonance wavelengths. In this context, we have performed a number of simulations assuming the resonance wavelength misaligned, as induced by the fabrication error $\Delta\Lambda$. We have quantified that effect and have found with simulations that the actual resonance wavelength of a Type I MZI will experience a deviation from λ_o by an amount $\Delta\lambda$ due to such errors. The specific result is $\Delta\lambda = 2.8\ \Delta\Lambda$. The likely scenario is the one in which errors occur in the same direction within the two MZI arms, and then the switch's passband center-wavelength shifts away from the design wavelength λ_o where the input light operates.

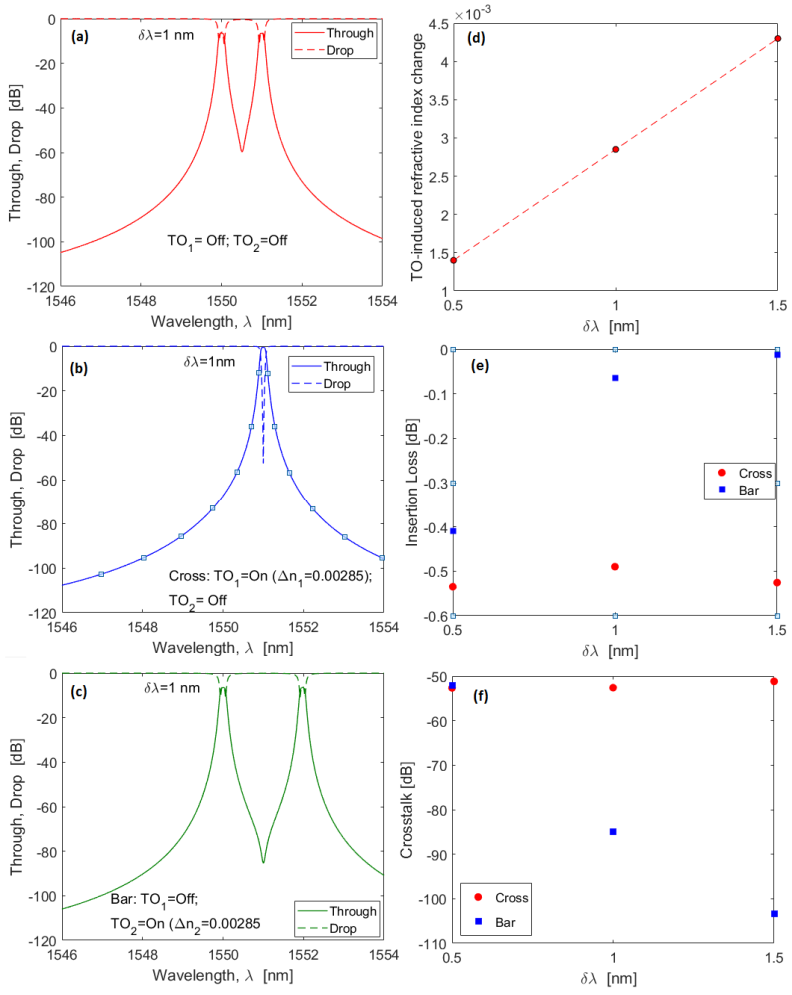

Fig. 4. Type-II Through and Drop spectra for $N = 3$, $M = 30$, and $W_t = 100$ nm; (a) All TOs are switched-off; (b) Cross state: TO_1 switched-on and TO_1 switched-off; (c) Bar state:TO_1 switched-off and TO_2 switched-on; (d). TO-induced refractive index change needed for Cross as a function of $\delta\lambda$ selection, (e) Insertion loss for Cross and Bar states as a function of $\delta\lambda$; (f) Crosstalk for Cross and Bar states as a function of Δn .

Optics EXPRESS

As a result, the IL and CT in the cross state are reduced by an amount that depends upon the switch BW. Our judgement is that a fabrication error of 0.04% is the largest that could be accepted in order to maintain good performance metrics.

As mentioned above, an increase in period values Λ generally induces an increase of the center wavelength of the resonance. However, it is interesting to consider the grating periods that induce the higher-order Bragg condition $\Lambda = m\lambda / 2n_{eff}$ (with m the grating order). Indeed, in our case, all of the period values Λ_m equal to $m \times 315$ nm induce the same 1550-nm resonance. Beneficially, these larger grating periods reduce the influence of fabrication errors. However, the MZI footprint becomes larger although with faster filter roll-off. In the following we argue that the additional detrimental effects induced by the silicon thermal expansion can be consider negligible. Indeed, the temperature increase required to obtain $\Delta n = 0.004$ is about 21.5 °C. As a result, assuming the silicon thermal expansion coefficient $\alpha_{th} = 3.6 \times 10^{-6}$ K^{-1}, we record a thermally induced period change of about 0.024 nm, which means 0.076% change. Similarly, this increase in temperature induces a change in the Bragg section length evaluated as $\Delta LB_1 = 0.61$ nm and $\Delta LB_2 = 0.71$ nm in the case of $N = 3$. Although ΔLB_1 and ΔLB_2 induce deviations from the designed values listed in Table 2, our simulations indicate that they are small enough to avoid influence on the Butterworth response. Finally, we guess that a power consumption ranging between 2.5 and 3.5 mW could be required to tune the proposed filters.

At this point in the paper, we shall change the focus to examine the tunable-filter opportunities. The narrowband Type I MZI is a continuosly tunable filter, and we have found that when two such filters are connected in an optical series arrangment or "cascade" that a variety of filter profiles is feasible at the cascade output ports. These cascaded filters will be the subject of a future paper, but we can present a schematic preview here. The simplest arrangment is two "slightly different" MZI Type I filters connected as shown in Figs. 5(a) and 5(b). The quantitive results of our analysis will be presented subsequently, but we can say qualitatively that the spectral profiles of the composite filter can consist of two peaks or two notches with tunable spacings and wavelength locations. Also feasible is a movable passband containing a tunable notch. We also found that a group of filter-MZIs can be interconnected into the form of a rectangular M x N mesh that includes some broadband crossbar switches for mesh reconfiguration. The result is a multiple-signal optical processing network functioning as a programmable and reconfigurable optical filter bank [29].

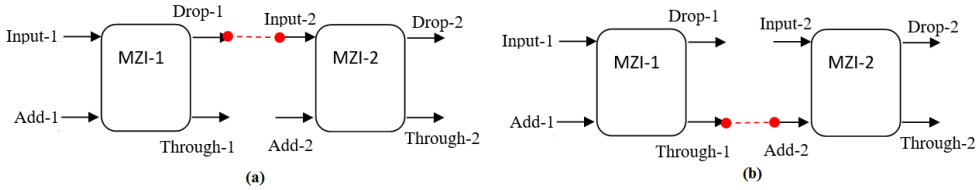

Fig. 5. One row of the proposed multi-row reconfigurable filter-cascade mesh. The example of the 2-cascade of resonant 2 x 2 TO MZI bulding blocks is shown.

4. Performance comparison

How do our grating filter/switch structures compare with their corresponding nanobeam structures? Each structure includes a 1D photonic lattice, and in a first approximation, the periodicity or spacing of the lattice is fixed rather than being varied along the waveguide long axis. The periodicity is determined by the desired center wavelength of the resonance. An array of air holes or oxide-filled holes is used in the NBR, whereas in the WBR the side corrugations of waveguide material, also known as "teeth", form the array. The consequences of choosing a particular array length are similar in both WGR and NBR. Typically, in the

Optics EXPRESS

NBR, a "zero- point-defect cavity" is utilized and this is constructed by tapering the diameter of the holes along the long axis; an up-taper followed by a down-taper. By contrast, the WGR uses a fixed, finite-width cavity defined by a π-phase-shift "segment." The possibilities for engineering the teeth in the WBR are slightly larger than the possibilities of engineering the hole size in the NBR because in the WBR the teeth can extend beyond the fixed single-mode width W of the unperturbed strip waveguide, or they can be indentations of W,[∞] or they can be a mixture of positive and negative teeth; outside-and-inside. To be specific, we found in our simulations that "outside teeth" consistently gave the best performance. Looking at other features, the waveguided mode clings closer to the strip center line in the NBR than in the WBR.

The WBR offers an advantage in the photomasks used to manufacture the device because the WBR has uniform-size teeth as compared to the tapered sizes used in NBR. Moreover, although the footprint of our device is larger than that proposed in [11], our data record a significant improvement in the crosstalk for the cross state. Generally, the cross and bar performances predicted in Table 3 exceed those of the various nanobeam cases reported in the literature. If we compare the Fig. 3 behavior with the spectral response of the N = 2 coupled nanobeams in [11] they found oscillations induced in the Drop spectrum having maxima and minima around −18.5 dB and −25 dB with-18.5 dB CT at resonance; whereas our simulations do not show any oscillations and only an absolute minimum is observed in our Drop response. This feature is induced by the opportune choice of the WBR lengths, LB_i (see Table 2), realizing the maximally flat spectral response.

In the Butterworth filter design, important for coupling, where the N resonators are generally different from one another, the WBR version has an advantage over the NBR version because the WBR uses simple extensions of uniform-grating length whereas the NBR requires revised hole-tapering profiles in the modified resonators. Thus, since the maximally flat filter response requires perfect matching with the Butterworth polynomial coefficients, we guess that it is more complicated to design the NBR tapering profiles than the WBR LB_i (see Table 2). A detailed comparison of our WBR 2x2 with two, prominent prior-art NBR 2x2 MZI switches is presented in Table 5.

Table 5. Comparison between WBR-MZI and NBR-MZI

Values	NBR-MZI Ref [6]. (experimental)	NBR-MZI Ref [11]. (theoretical)	WBR-MZI Our work (theoretical)
Resonator number	N = 2	N = 2	N = 3 or 4
BW	99 GHz	28.18 GHz	18.7 GHz
Roll-off	-	73 dB/nm	150.5 dB/nm
Insertion Loss (Cross state)	–0.5 dB	–0.5 dB	–0.48 dB
Crosstalk (Cross state)	–22 dB	–18.5 dB	–52.7
Insertion Loss (Bar state)	–0.4 dB	–0.3 dB	–0.01 dB
Crosstalk (Bar state)	–22 dB	–28.7 dB	–50.5 ÷ –75.6 dB
Footprint	small	small	medium
Tuning	TO	TO	TO
Power consumption	Low	Low	Low/medium depending on N
Butterworth response	Medium/high complication for N>2	Medium/high complication for N>2	Low complication

At this point, it is interesting to perform a comparison with other resonant MZI structures, specifically, the low-power silicon electro-optic (EO) switch consisting of a double-ring-assisted Mach–Zehnder interferometer (DR-MZI) 2x2 crossbar [30-31], where active tuning elements based on p-i-n diodes and silicon resistive micro-heaters embedded in the microrings were employed for high-speed EO switching and low-loss thermo-optic (TO) tuning. A detailed comparison of our grating switch with the micro-ring assisted switches is given in Table 6.

Optics EXPRESS

Table 6. Comparison between WBR-MZI and DR-MZI

Values	DR-MZI Ref [31]. (experimental)	WBR-MZI Our work (theoretical)
BW	56 GHz	18.7 GHz
Δn	7.31×10^4	0.0015
Crosstalk	−50 dB	−52.7 dB
Footprint	medium	medium
Tuning	EO switching + TO tuning	TO
Power consumption	Low	Low/medium depending on N
Butterworth response	-	Yes

5. Conclusions

In this paper a mixed full-vectorial mathematical model based on the FEM, CMT and Transfer Matrix approaches has been implemented for investigating the performance of integrated-photonic single and cascaded 2x2 Mach–Zehnder optical switches, where each arm of the interferometer is composed of N-coupled Bragg resonators deployed in one single-mode SOI waveguide that operates around 1550 nm. Simulations indicate that fully-etched strip waveguides are more suitable than rib waveguides for achieving efficient crossbar-and-tunable switching by means of a thermo-optic Δn heater stripe formed on the top of each interferometer arm. The length of the coupled Bragg resonator array has been opportunely designed to induce maximally flat spectral response. The N-coupling approach with $N \leq 4$ is found to be a valuable tool for attaining high-quality switch passbands and fairly small switch footprint. Using the Butterworth filter design and extending the silicon teeth laterally beyond the 450-nm width of the silicon single-mode channel waveguides allows us to perform grating engineering that yields very steep side walls on the Bragg filter spectral profile, with a filter bandwidth that is readily engineered to be in the 5 to 200 GHz range.

Taking a TE_{00} polarization for the input light, output spectra at the Through and Drop ports have been computed, and the IL and CT metrics are found to be excellent at both low and medium TO drive levels, for example −0.48 dB IL and −52.7 dB CT and −0.002 dB IL and −75.6 dB CT for the Cross and Bar states, respectively. Generally, these projections represent a major improvement in the switching art. We have also proposed Type I and Type II addressing of the TO heaters and have found similar crossbar IL and CT metrics for the two methods. Finally we examined the possibilites of tunable narrowband optical filtering that can be achieved by connecting the Type I MZIs in an optical cascade. We looked at several interconnections. A variety of pass or block filters with wide TO tunability appears feasible, and a reconfigurable “mesh” of MZIs can be constructed to give a programmed selection of many filter profiles at the output ports, including very narrowband filters if desired.

The resonant nature of the 2 x 2 crossbars necessitates tradeoffs in an on-chip N x N routing matrix made from those elements. Nevertheless, in the context of wavelength-division systems, we conclude that our N-coupled-Bragg MZIs have great potential for practical high-perfomance applications in which ultralow (EO) energy and reasonably small footprint are important. The tunable filter-cascade meshes proposed and analyzed here appear to have high potential for on-chip applications in microwave photonics and optical sensing.

Funding

Fondo per il finanziamento delle attività base di ricerca (MIUR FFABR 2017); Air Force Office of Scientific Research (FA9550-17-1-0354).